Light-Matter Interaction Enhancement in Anisotropic 2D Black Phosphorous via Polarization-Tailoring Nano-Optics

Nima Sefidmooye Azar,[†] James Bullock,[†] Sivacarendran Balendhran,[‡] Hyungjin Kim,[¶,§] Ali Javey,[¶,§] and Kenneth B. Crozier[*,†,‡,‖]

[†]*Department of Electrical and Electronic Engineering, University of Melbourne, Victoria 3010, Australia*

[‡]*School of Physics, University of Melbourne, Victoria 3010, Australia*

[¶]*Department of Electrical Engineering and Computer Sciences, University of California, Berkeley, CA 94720, USA*

[§]*Materials Sciences Division, Lawrence Berkeley National Laboratory, Berkeley, CA 94720, USA*

[‖]*ARC Centre of Excellence for Transformative Meta-Optical Systems, University of Melbourne, Victoria 3010, Australia*

E-mail: kcrozier@unimelb.edu.au

Abstract

Black phosphorous (bP), a two-dimensional (2D) layered material, has shown great potential for infrared (IR) optoelectronics owing to the narrow and direct bandgap it exhibits when in multilayer form. However, its thinness and optical anisotropy lead to weak light absorption, which limits the performance of bP-based photodetectors. In this work, we explore plasmonic nanoantennas, optical cavities, and their hybrids that

can be integrated with multilayer bP to enhance its light absorption. This is achieved by near-field light intensity enhancement and polarization conversion. In addition, we demonstrate that these nanostructures can boost the spontaneous emission from bP. Light absorption enhancements of up to 185 and 16 times are obtained for linearly polarized and unpolarized IR light, respectively, in comparison with a commonly used device architecture (bP on SiO_2/Si). Moreover, IR light emission enhancements of up to 18 times are achieved. The optical nanostructures presented here can be exploited for enhancing the detectivity of photodetectors and electroluminescence efficiency of light-emitting diodes based on bP and other 2D materials.

Keywords

bP, plasmonic nanoantennas, optical cavities, infrared (IR) light absorption and emission, Purcell effect, 2D layered materials

Introduction

Optical nanoantennas can confine light in deeply subwavelength volumes leading to strong near-field intensity enhancements. In a reciprocal manner, they can boost the luminescence of emitters placed in their vicinity. Hence, they have been widely employed for light-matter interaction enhancement in surface-enhanced Raman scattering,[1,2] surface-enhanced fluorescence,[1,3] surface-enhanced infrared absorption,[4] and more recently, optoelectronic devices based on two-dimensional (2D) materials.[5–8]

Owing to their exceptional properties, 2D layered materials including graphene, black phosphorous (bP), and transition metal dichalcogenides (TMDs, *e.g.* MoS_2 and WSe_2) have proven to be promising candidates for optoelectronic devices.[9–12] Photodetectors,[13–16] light-emitting diodes (LEDs),[17–19] and optical modulators[20,21] based on these materials have been demonstrated. However, a major challenge for optoelectronics based on 2D materials is their

low light absorption, resulting from their thinness and thus short optical interaction path. Furthermore, high non-radiative decay rates lead to inefficient emission from 2D materials. This has motivated the use of optical structures such as plasmonic[22–33] and dielectric[34] nanoantennas and optical cavities[35–39] for light absorption and emission enhancement in these materials. These studies have mainly focused on light absorption enhancement in monolayer graphene[7,8,20,23,24,37] and photoluminescence enhancement in monolayer MoS_2,[28,29,33] WS_2,[25,27,30] and WSe_2.[31,32,34,38]

Infrared (IR) detectors and emitters play a pivotal role in a variety of areas including biomedical and thermal imaging, spectroscopy, gas sensing, telecommunication, night vision, and astronomy. Multilayer bP is particularly suitable for mid-wave IR applications thanks to its direct and narrow bandgap of $\sim$0.31 eV.[40,41] Additionally, it forms a high-quality p-n heterojunction with MoS_2 which is suitable for IR photodiodes[42–45] and LEDs.[46]

Some 2D materials such as bP[47] and quasi-2D Te[35] possess an anisotropic crystal structure leading to optical anisotropy. For instance, bP has an armchair atomic arrangement along one in-plane direction and a zigzag arrangement along the other. The optical absorption and emission in the armchair direction are much stronger than those in the zigzag direction.[42,46,48] Although this property can be exploited for polarization detection[42] and polarization imaging,[49] in general, it is not desirable. For example, photodetectors based on bP are nearly blind to one polarization. This also means that the power carried by one polarization cannot be collected when detecting unpolarized light.

Herein, we explore plasmonic nanoantennas, optical cavities, and their combinations for enhancing the light-matter interaction in multilayer bP in the IR region. Finite-difference time-domain (FDTD) electromagnetic simulations were performed to this end. These optical nanostructures boost the light absorption in bP by intensifying the local electromagnetic fields. In a reciprocal manner, they enhance the light emission from bP by accelerating its spontaneous emission rate. We demonstrate that plasmonic nanoantennas can be utilized for tailoring the near-field light polarization and thus engineering the optical isotropy of

2D materials. T-shaped nanoantennas can convert the light polarization from the zigzag to armchair crystal direction and hence create a nearly isotopic light absorption in bP. T-shaped nanoantennas were previously proposed as a bimodal antenna structure with two independent resonances localized in a single nanogap. They can be used for coupling with quantum emitters that show a shift between absorption and emission frequencies.[50]

Results and discussion

Light absorption in 2D materials can be boosted by integrating them with plasmonic nanoantennas and optical cavities. This originates from the light confinement and intensity enhancement provided by the optical structure. The time-averaged optical power density absorbed in a material can be expressed as[51]

$$\langle \overrightarrow{E(t)} \cdot \frac{\partial \overrightarrow{P(t)}}{\partial t} \rangle = \frac{1}{2}\omega \sum_{j=x,y,z} \epsilon_j'' E_j^2 = \epsilon_0 \omega \sum_{j=x,y,z} n_j k_j E_j^2 \quad (1)$$

where $\vec{E} = E_x\hat{x} + E_y\hat{y} + E_z\hat{z}$ denotes the electric field, $\vec{P}$ electric polarization, ω angular frequency, $\epsilon = \epsilon' + \mathrm{i}\epsilon'' = \epsilon_0(n + \mathrm{i}k)^2$ material's permittivity, and ϵ_0 vacuum permittivity. According to this equation, the optical power absorbed in the material associated with each direction is proportional to the electric field intensity, n, and k in that direction.

The crystal structure of bP is visualized in Figure 1a. The armchair and zigzag crystal directions are defined as x and y, respectively. The optical anisotropy of bP can be seen in Figure 1b, which shows the complex refractive index $(n + \mathrm{i}k)$ of multilayer bP along the different crystal directions. The experimentally measured in-plane (x and y) and theoretically calculated out-of-plane (z) refractive index values were taken from refs. (42) and (52), respectively. For energies above the armchair band edge of ∼0.31 eV ($\lambda = 4$ μm), k_x is much larger than k_y and k_z which results in much stronger light absorption associated with the x direction.

The armchair bandgap of bP saturates to its bulk value of ∼0.31 eV for flakes thicker than

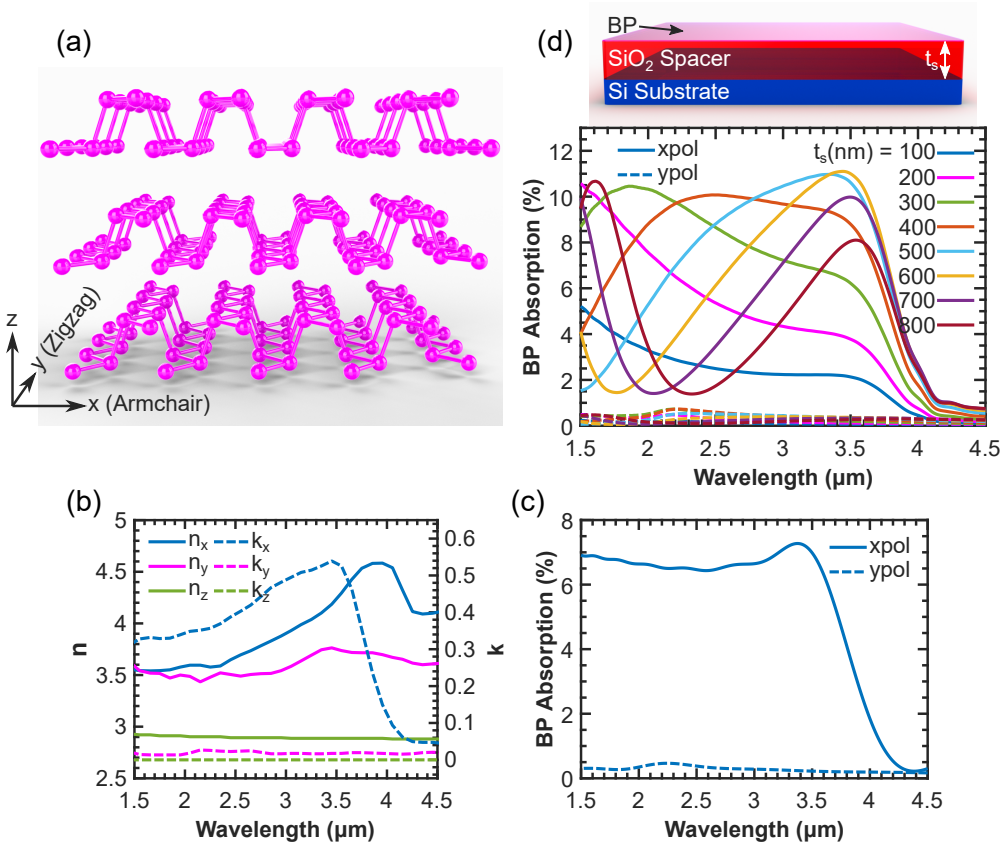

Figure 1: (a) Schematic of bP crystal structure. (b) Complex refractive index of bP taken from refs. (42) and (52). (c) Optical power absorbed in suspended 10-nm-thick bP ("Suspended" structure) with the incident light polarized in the x (armchair) and y (zigzag) directions. (d) Schematic of 10-nm-thick bP sitting on the SiO_2/Si substrate ("SiO_2/Si" structure) and optical power absorbed in bP with different SiO_2 thicknesses for x- and y-polarized light.

4 nm (∼8 layers).[53] A bP flake with thickness of 10 nm was considered in all the following simulations. Figure 1c plots the optical power (normalized to the source power) absorbed in a suspended 10-nm-thick bP flake as a function of wavelength with the incident light polarized in the x and y directions. This configuration is referred to as "Suspended" here. As expected, the absorption for x-polarized light is much greater than that for y-polarized light.

Optoelectronic devices based on 2D materials are often fabricated on SiO_2/Si substrates, as illustrated in Figure 1d. The SiO_2 layer electrically insulates the 2D material sitting on the substrate from Si, which can also be used to apply a gate bias. Figure 1d plots the power absorbed in a 10-nm-thick bP sitting on this substrate (referred to as "SiO_2/Si"

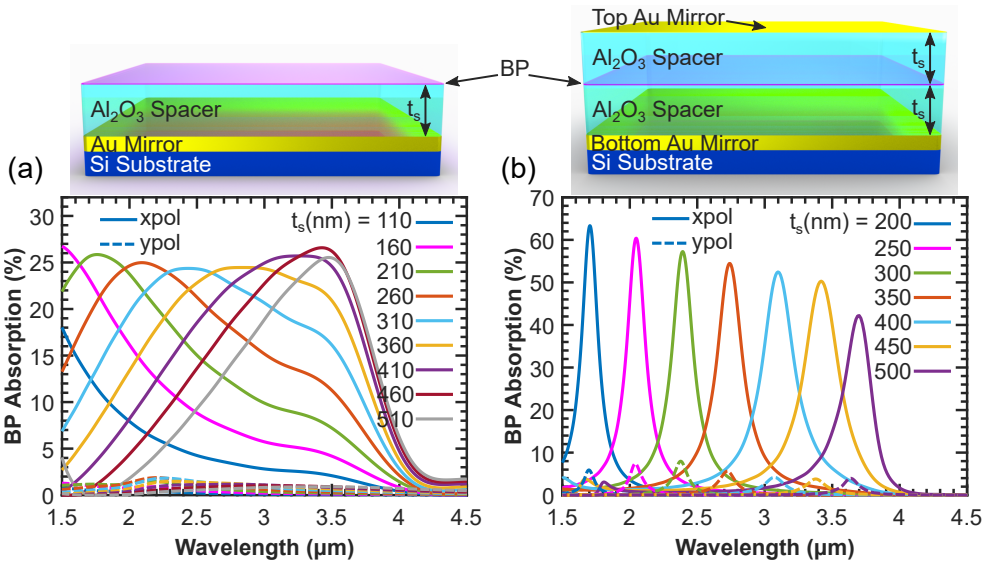

Figure 2: (a) Schematic of 10-nm-thick bP sitting on the Al_2O_3/Au optical cavity substrate ("Half-Cavity" structure) and optical power absorbed in bP with varying Al_2O_3 thickness for x- and y-polarized light. (b) Schematic of 10-nm-thick bP placed in the FP cavity ("FP Cavity" structure) and optical power absorbed in bP with different spacer thicknesses for x- and y-polarized light.

structure here) with different SiO_2 thicknesses (t_s) for x- and y-polarized light. The SiO_2/Si stack acts as an optical cavity; the reflected light from the SiO_2/Si interface interferes with the incident light at the substrate surface. This gives rise to the resonance observed in the absorption spectrum which redshifts with an increase in t_s. We note that t_s can be optimized for bP absorption; however, other studies usually use an SiO_2 thickness of 300 nm[19,26,28,41,43] or less,[8,16,22,27,29,44,46,48] regardless of the operating wavelength. Accordingly, here we benchmark the other structures against the "SiO_2/Si; $t_s = 300$ nm" configuration.

Light intensity at the substrate surface can be increased by using a metallic mirror. Here we consider the Al_2O_3/Au optical cavity substrate shown in Figure 2a, which consists of a 120-nm-thick Au mirror and an Al_2O_3 layer with thickness t_s on an Si substrate. Here, the Al_2O_3 layer acts as the optical spacer and electrical insulator. The reflected light from the Au mirror interferes constructively with the incident light at the substrate surface leading to light intensity enhancement. To maximize the light intensity at the substrate surface at wavelength λ, t_s should be equal to $\lambda/(4n_s)$, where n_s is the refractive index of the spacer.

Figure 2a presents the power absorbed in the 10-nm-thick bP sitting on this substrate (termed "Half-Cavity" structure here) with varying Al_2O_3 thickness for x- and y-polarized light. The bP absorption in this structure is greater than that in "SiO_2/Si" for both polarizations.

A Fabry-Pérot (FP) cavity can further enhance the bP absorption. It is formed by adding a spacer/mirror stack on top of bP in the "Half-Cavity" structure. The resulting configuration ("FP Cavity"), along with bP absorption for different spacer thicknesses (t_s) and polarizations, is depicted in Figure 2b. In this structure, the incident light penetrates through the thin, semi-transparent top Au mirror and resonates between the two mirrors at $\lambda \approx 4t_s n_s$ (fundamental resonance). The thickness of the top Au mirror (t_m) was optimized for the unpolarized light absorption, which is $abs_{unpol} = (abs_{xpol} + abs_{ypol})/2$. For example, for $t_s = 400$ nm, the optimal top mirror thickness is $t_m = 4$ nm. The optimal t_m for other t_s values is reported in the Supporting Information, Table S1. This configuration provides a stronger absorption with a narrower bandwidth than the "Half-Cavity" and "SiO_2/Si" configurations for both polarizations. *E.g.*, for $t_s = 400$ nm, the full width at half maximum is 282 nm for x-polarized light, which is ~5.6 times smaller than that for "Half-Cavity; $t_s = 410$ nm" (1590 nm). Yan *et al.* recently employed a similar device architecture for spectrally selective IR detection based on bP/MoS_2 photodiodes.[45]

As seen above, optical cavities can significantly enhance the bP absorption. However, the absorption for y-polarized light is still much smaller than that for x-polarized light due to the optical anisotropy of bP. Plasmonic nanoantennas can effectively manipulate the optical near fields. In addition to strongly confining light and thus enhancing the near-field intensity, they can modify the near-field polarization. We found T-shaped nanoantennas particularly useful for this purpose. Figure 3a illustrates the "T-Shaped" configuration, which is formed by integrating periodically arranged T-shaped Au nanoantennas with the "Half-Cavity" structure. Geometrical parameters of T-shaped nanoantennas are depicted in Figure 3b. The antenna gap is aligned in the x (armchair) direction. Figure 3c plots the optical power absorbed in bP with varying l_x for x- and y-polarized incident light. Antenna

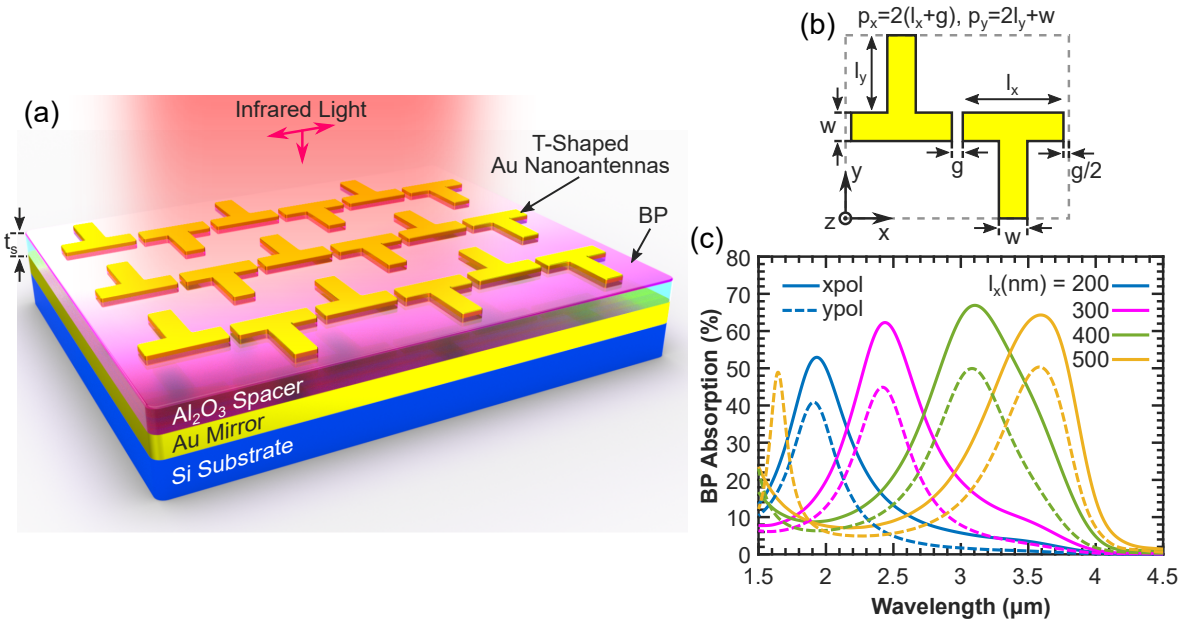

Figure 3: (a) Schematic illustrating 10-nm-thick bP sitting on the Al_2O_3/Au optical cavity substrate integrated with periodic T-shaped Au plasmonic nanoantennas ("T-Shaped" structure). (b) Geometrical parameters of T-shaped nanoantennas. The gray dashed box represents the unit cell. p_x and p_y are the period in the x and y directions, respectively. (c) Optical power absorbed in bP with varying l_x for x- and y-polarized illumination.

thickness and gap (g) were set to 30 nm and 40 nm, respectively, in all the simulations in this work. We found that the performance of plasmonic structures deteriorates with further increase of these parameters. Other parameters (l_y, t_s, and w) were optimized for unpolarized light absorption. *E.g.* for $l_x = 400$ nm, we have $(l_y, t_s, w) = (290, 120, 120)$ nm. Optimal parameters for other l_x values are reported in the Supporting Information, Table S2. High absorption values are achieved for both polarizations. For instance, for $l_x = 400$ nm, bP absorption is 66.76% and 49.94% for x- and y-polarized illumination, respectively, at $\lambda = 3.08$ μm. This is a huge enhancement in comparison with previous configurations, especially for y-polarized illumination.

Figure 4 provides insights into the absorption enhancement mechanism in the "T-Shaped" configuration. Figure 4a presents the light absorption density in bP, calculated using equation (1), with $l_x = 400$ nm for x-polarized illumination at $\lambda = 3.08$ μm. Results for y-polarized illumination are shown in Figure 4b. The arrows represent the in-plane component

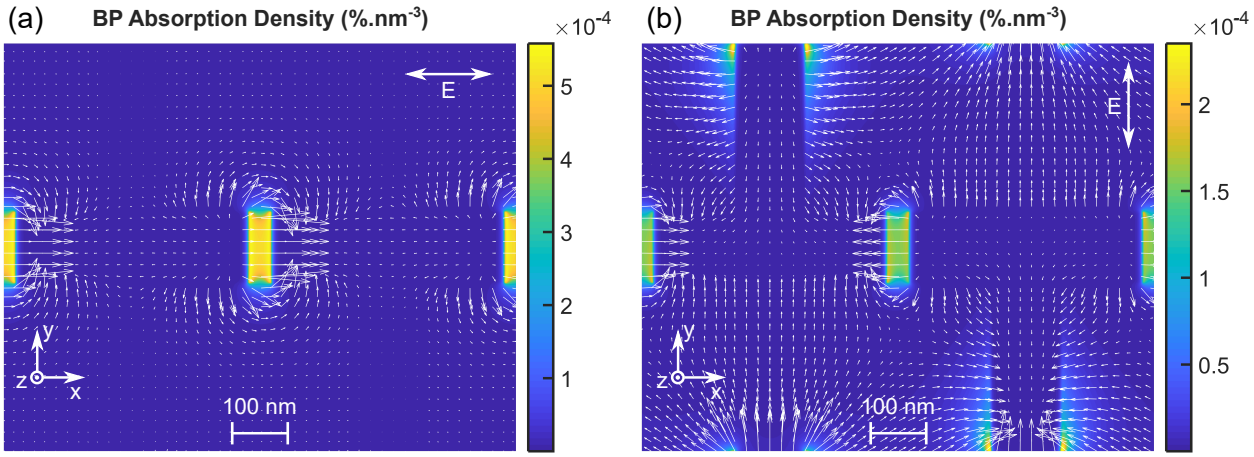

Figure 4: Light absorption density in bP in the "T-Shaped" structure with $l_x = 400$ nm for (a) x-polarized and (b) y-polarized incident light at $\lambda = 3.08$ μm. The arrows represent the in-plane component of electric field $(E_x\hat{x} + E_y\hat{y})$ at an instant of time. The absorption density and electric field values depicted here are the average values across the thickness of bP.

of electric field $(E_x\hat{x} + E_y\hat{y})$ at an instant of time. The absorption density and electric field values depicted here are the average values across the 10-nm thickness of the bP. For x-polarized illumination, T-shaped nanoantennas act like regular rod nanoantennas; they enhance the light intensity and thus absorption in the antenna gap through localized surface plasmon resonances. For y-polarized illumination, in addition to intensity enhancement, the T-shaped nanoantennas rotate the polarization to the x direction (along which bP can absorb light) in the gap and around the T legs.

Periodic rod nanoantennas, as shown in Figure 5a, can be used for polarization dependent absorption enhancement in 2D materials. Integrating them with the "Half-Cavity" structure and optimizing the geometrical parameters for x-polarized light absorption in bP led us to ribbon nanoantennas, *i.e.* $p_y = w$, as shown in Figure 5b. The resulting structure is referred to as "Ribbon" here. Optical power absorbed in bP in "Ribbon; $(l_x, t_s) = (280, 80)$ nm" is plotted in Figure 5c for x- and y-polarized incident light. Figure 5d presents the light absorption density in bP and the in-plane electric field in this structure for x-polarized illumination at $\lambda = 3.08$ μm. In addition to enhancing the absorption for x-polarized light, this structure strongly suppresses the absorption for y-polarized light. The metallic ribbons

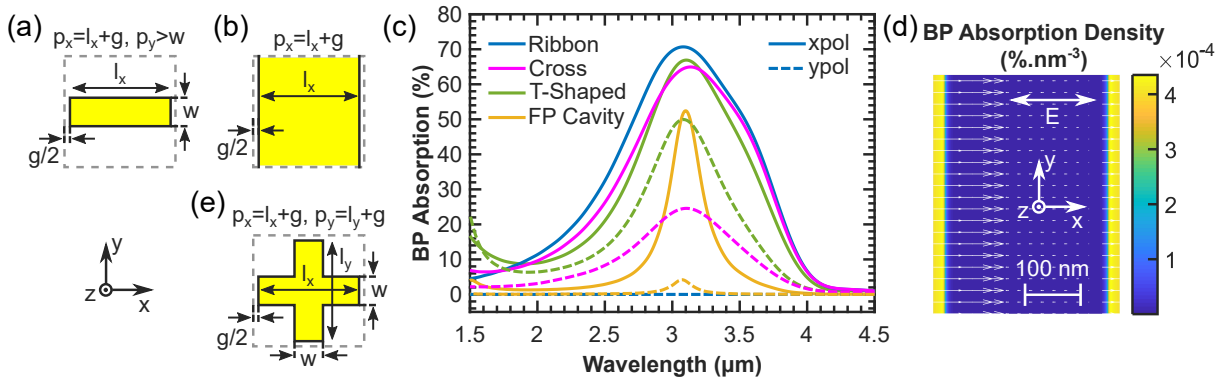

Figure 5: (a) and (b) Geometrical parameters of periodic rod and ribbon Au nanoantennas, respectively. (c) Optical power absorbed in bP in the "Ribbon; $l_x = 280$ nm", "Cross; $l_x = 360$ nm", "T-Shaped; $l_x = 400$ nm", and "FP Cavity; $t_s = 400$ nm" structures for x- and y-polarized incident light. (d) Light absorption density in bP in the "Ribbon; $l_x = 280$ nm" structure for x-polarized incident light at $\lambda = 3.08$ μm. The arrows represent the in-plane component of electric field ($E_x\hat{x} + E_y\hat{y}$) at an instant of time. The absorption density and electric field values depicted here are the average values across the thickness of bP. (e) Geometrical parameters of periodic cross-shaped Au nanoantennas. In (a), (b), and (e), the unit cell is marked by a gray dashed box. p_x and p_y are the period in the x and y directions, respectively.

do not resonate for y-polarized illumination and shadow the underlying bP. The y-polarized light cannot penetrate through the 40-nm antenna opening either, as its electric field is parallel to the metallic features in the gap. This is further illustrated in the Supporting Information, Figure S1, which depicts the electric field intensity (normalized to the incident intensity) inside bP (averaged across its thickness) for x- and y-polarized illumination. The light intensity ($|E|^2/|E_i|^2$) is smaller than 10^{-10} everywhere inside bP (including the gap area) for y-polarized illumination. Hence, this configuration can be used for creating strongly anisotropic optical response in 2D materials.

Polarization independent absorption enhancement in 2D materials can be achieved employing periodic cross-shaped nanoantennas, as shown in Figure 5e. The configuration obtained by integrating these nanoantennas with the "Half-Cavity" structure is termed "Cross" here. Figure 5c compares the optical power absorbed in bP in the "Cross; $(l_x, l_y, t_s, w) = (360, 370, 120, 120)$ nm", "Ribbon; $l_x = 280$ nm", "T-Shaped; $l_x = 400$ nm", and "FP Cavity; $t_s = 400$ nm" configurations for x- and y-polarized illumination. The Supporting Informa-

Table 1: BP absorption at $\lambda = 3.08$ μm for different configurations optimized for this wavelength

	abs_{xpol} (%)	abs_{ypol} (%)	abs_{unpol} (%)	abs_{xpol}/abs_{ypol}
Suspended	6.72	0.28	3.5	24
SiO_2/Si; $t_s = 300$ nm	7.08	0.27	3.68	26.22
Half-Cavity; $t_s = 410$ nm	25.43	1.05	13.24	24.22
FP Cavity; $t_s = 400$ nm	51.79	4.14	27.97	12.51
T-Shaped; $l_x = 400$ nm	66.76	49.94	58.35	1.34
Ribbon; $l_x = 280$ nm	70.68	$< 10^{-10}$	35.34	$> 7 \times 10^{11}$
Cross; $l_x = 360$ nm	64.46	24.51	44.49	2.63

tion, Figure S2, presents the light absorption density in bP and the in-plane electric field in the "Cross; $l_x = 360$ nm" structure for x- and y-polarized incident light at $\lambda = 3.08$ μm. The "Cross" structure provides a higher absorption for y-polarized illumination compared with "FP Cavity". However, it is lower than that provided by the "T-Shaped".

To summarize the results, Table 1 lists the bP absorption values at $\lambda = 3.08$ μm for different optical structures optimized for this wavelength. The "T-Shaped" configuration exhibits the highest absorption for y-polarized (abs_{ypol}) and unpolarized (abs_{unpol}) illumination. It enhances abs_{ypol} by 185 times and abs_{unpol} by 16 times in comparison with the commonly used "SiO_2/Si" structure. The "Ribbon" structure shows the highest absorption for x-polarized illumination (abs_{xpol}), the lowest abs_{ypol}, and the highest anisotropy (abs_{xpol}/abs_{ypol}). It enhances abs_{xpol} by 10 times, suppresses abs_{ypol} by more than 10^9 times, and enhances abs_{xpol}/abs_{ypol} by more than 10^{10} times compared with "SiO_2/Si".

In addition to light absorption enhancement, optical nanoantennas and cavities can enhance the light emission from emitters located in their electromagnetic environment. This mainly arises from the enhancement of emitter's spontaneous emission rate, which is known as Purcell effect.[54,55] The spontaneous emission rate is proportional to the local density of states in the emission process, which is proportional to the emitted power. The latter quantity can be calculated by classical FDTD simulations. Here, we studied the emission enhancement in the 10-nm-thick bP integrated with different optical structures. The emission process was modelled using a broadband oscillating electric dipole polarized in the x

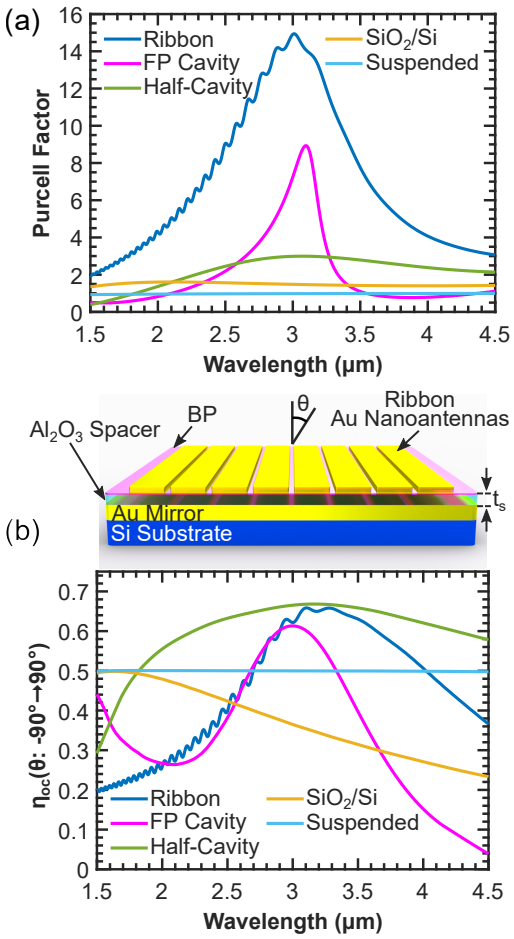

Figure 6: (a) Purcell enhancement factor and (b) out-coupling efficiency to the upper half-space for "Ribbon; $l_x = 280$ nm", "FP Cavity; $t_s = 400$ nm", "Half-Cavity; $t_s = 410$ nm", "SiO_2/Si; $t_s = 300$ nm", and "Suspended" structures. Panel b includes a schematic of the "Ribbon" structure depicting the collection angle θ.

(armchair) direction, which was positioned in the middle layer of the 10-nm-thick bP.

Purcell factor (f_P) is defined as the spontaneous emission rate enhancement provided by the optical medium. *I.e.*, $f_P = \gamma_r/\gamma_r^0$, where γ_r and γ_r^0 are the radiative decay rates of excitons in the optical structure and in a homogeneous medium, respectively. Figure 6a plots the Purcell factor for the "Ribbon; $l_x = 280$ nm", "FP Cavity; $t_s = 400$ nm", "Half-Cavity; $t_s = 410$ nm", "SiO_2/Si; $t_s = 300$ nm", and "Suspended" structures. The "Ribbon" structure yields the highest f_P. Multiple ribbons were used for simulating the emission process in the "Ribbon" structure, which results in the multiple resonance peaks in the f_P curve.

Out-coupling efficiency (η_{oc}) is the fraction of radiated photons that manage to escape the

optical structure and reach a desired range of angles θ, as shown for the "Ribbon" structure in Figure 6b, in the far field. This figure plots $\eta_{oc}(\theta\text{: } -90^\circ \rightarrow 90^\circ)$, *i.e.* out-coupling efficiency to the upper half-space, for different configurations. At $\lambda = 3.08$ μm, "Half-Cavity" yields the highest η_{oc} of 67.6%. The rest of the emitted light is mainly waveguided through the Al_2O_3 spacer in the horizontal direction. In the "SiO_2/Si" configuration, in addition to the horizontally waveguided light, a considerable portion of the photons is radiated downwards and hence lost. This leads to a smaller $\eta_{oc}(\theta\text{: } -90^\circ \rightarrow 90^\circ)$ for this structure compared with the ones containing a bottom mirror.

The emission efficiency (η_e) of an optical structure can be defined as $\eta_e = \eta_q \eta_{oc}$. Here, η_q is the quantum efficiency which is the fraction of transitions from the excited states to the ground state that are radiative; *i.e.*, $\eta_q = \gamma_r/(\gamma_r + \gamma_{nr} + \gamma_l)$. In this relation, γ_{nr} is the decay rate of excitons to non-radiative channels such as phonons, and γ_l is the loss decay rate accounting for the non-radiative channels that the optical structure might introduce. The emission enhancement provided by the optical structure in comparison with a homogeneous medium can be expressed as $\eta_e/\eta_e^0 = (\eta_q/\eta_q^0) \times (\eta_{oc}/\eta_{oc}^0)$, where $\eta_q^0 = \gamma_r^0/(\gamma_r^0 + \gamma_{nr}^0)$ is the intrinsic quantum efficiency. Assuming $\gamma_{nr} = \gamma_{nr}^0$, for an intrinsically low-quantum efficiency emitter, *i.e.* $\gamma_{nr}^0 \gg \gamma_r^0$, η_q/η_q^0 can be approximated as

$$\frac{\eta_q}{\eta_q^0} \approx \frac{\gamma_r/\gamma_r^0}{1 + (\gamma_r + \gamma_l)/\gamma_{nr}^0}.$$

If $\gamma_{nr}^0 \gg (\gamma_r + \gamma_l)$, then the latter equation reduces to $\eta_q/\eta_q^0 \approx \gamma_r/\gamma_r^0 = f_P$. Hence, $\eta_e/\eta_e^0 \approx f_P \times (\eta_{oc}/\eta_{oc}^0)$. This leads us to $\eta_e^2/\eta_e^1 \approx (f_P^2/f_P^1) \times (\eta_{oc}^2/\eta_{oc}^1)$, which suggests that the quantity $f_P \times \eta_{oc}$ can be used for comparing the emission efficiency of different optical structures. The main assumption made here is that the emitter has a low intrinsic quantum efficiency which is the case for multilayer bP.[56] Figure 7a–e present the spectral and far-field angular distribution of this quantity, *i.e.* $f_P \times \partial\eta_{oc}/\partial\theta$, for the "Ribbon; $l_x = 280$ nm", "FP Cavity; $t_s = 400$ nm", "Half-Cavity; $t_s = 410$ nm", "SiO_2/Si; $t_s = 300$ nm", and

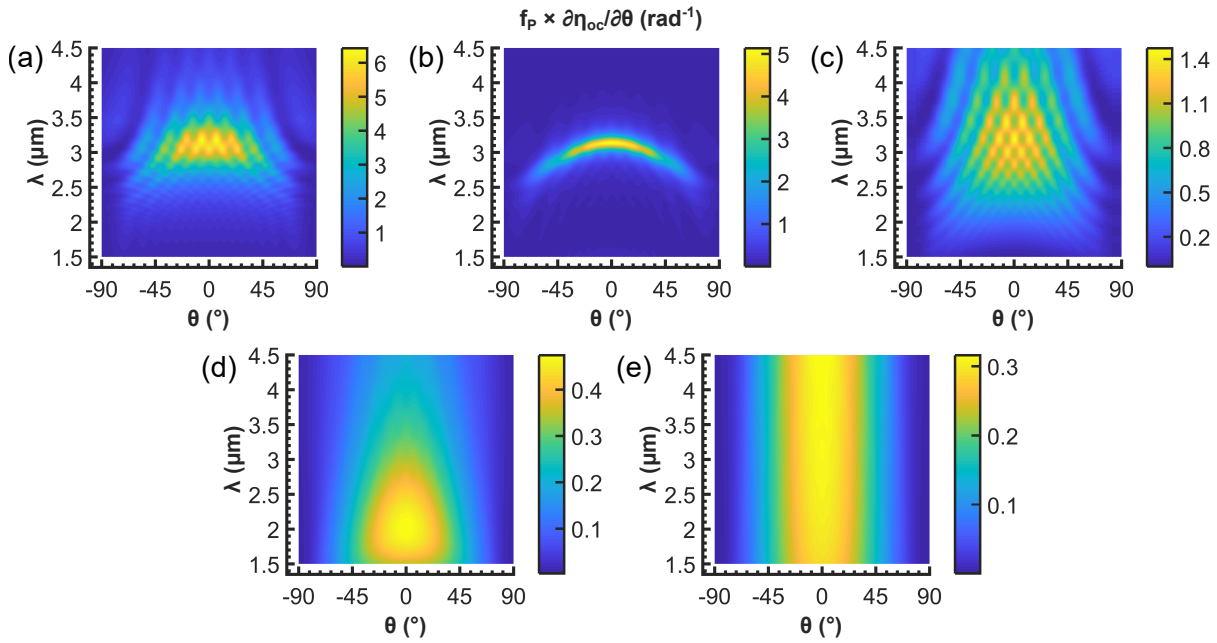

Figure 7: Spectral and far-field angular distribution of light emission efficiency for (a) "Ribbon; $l_x = 280$ nm", (b) "FP Cavity; $t_s = 400$ nm", (c) "Half-Cavity; $t_s = 410$ nm", (d) "SiO_2/Si; $t_s = 300$ nm", and (e) "Suspended" structures.

Table 2: Emission metrics at $\lambda = 3.08$ μm for different configurations optimized for this wavelength

	f_P	$\eta_{oc}(\theta\colon -90° \to 90°)$	$f_P \times \eta_{oc}(\theta\colon -90° \to 90°)$
Suspended	0.98	0.5	0.49
SiO_2/Si; $t_s = 300$ nm	1.47	0.35	0.52
Half-Cavity; $t_s = 410$ nm	2.99	0.68	2.02
FP Cavity; $t_s = 400$ nm	8.86	0.61	5.42
Ribbon; $l_x = 280$ nm	14.2	0.66	9.31

"Suspended" structures, respectively. Table 2 summarizes the emission metrics at $\lambda = 3.08$ μm for different optical structures optimized for this wavelength. The "Ribbon", "FP Cavity", and "Half-Cavity" configurations provide emission enhancements of 17.9, 10.4, and 3.9 times, respectively, in comparison with the commonly used "SiO_2/Si" structure.

Conclusion

In this work, we designed optical nanostructures including plasmonic nanoantennas, optical cavities, and their combinations for enhancing the interaction of IR light with multilayer bP. We demonstrated that T-shaped nanoantenna-cavity hybrid can efficiently enhance the light absorption in bP by boosting the light intensity and converting its polarization. It was also found that ribbon nanoantenna-cavity hybrid can simultaneously enhance and suppress the light absorption for different polarizations, and thus, enhance the optical anisotropy of 2D materials. Furthermore, these optical structures were found to considerably enhance the light emission from 2D materials through Purcell effect. BP and other 2D materials have great potential for optoelectronic applications, and their integration with the optical structures presented here can significantly boost the performance of devices based on these materials.

Methods

The finite-difference time-domain (FDTD) technique,[57] implemented in the Lumerical FDTD Solutions software package, was employed to solve the Maxwell's equations. To study the spectral response of the optical structures, we used a broadband (λ = 1.5–4.5 μm) light source in both absorption and emission simulations. The mesh size was 1 nm around the finest features. The experimentally measured wavelength-dependent complex refractive index values of Al_2O_3 and SiO_2 were taken from ref. (58), and those of Au and Si were taken from ref. (59).

In the absorption simulations, the light source was a linearly polarized plane wave at normal incidence. Perfectly matched layers (PMLs) were utilized to describe the boundary conditions in the light propagation direction. Periodic boundary conditions were implemented in the direction perpendicular to propagation. The optical power absorbed in bP was obtained by calculating the net power flow into a surface enclosing the bP flake. This is

equivalent to integrating the absorption density, given by equation (1), over the volume of the bP flake. Geometrical parameters were optimized through parameter sweeping. Details of the optimization are included in the Supporting Information.

In emission simulations, PML boundary conditions were used in all directions. The light source was an electric dipole, placed in the middle layer of bP and oscillating in the x (armchair) direction. The optical power emitted by the dipole was obtained by calculating the net power flow out of a surface enclosing the dipole. In the "Ribbon" structure, multiple ($\sim$100) ribbons were used to mimic the periodicity of the nanoantennas. Also, the horizontal position of the dipole source was swept in the middle unit cell beneath the Au ribbons and the gap between them, and the average results were reported. Due to theoretical issues with simulating dipole sources placed in dispersive media, the imaginary refractive index of bP was set to zero in the emission simulations.

Acknowledgement

This work was supported by the Defense Advanced Research Projects Agency (HR0011-16-1-0004) and by the Australian Research Council (DP180104141).

Supporting Information

This material is available free of charge via the Internet at http://pubs.acs.org. Optimized geometrical parameters of the "FP Cavity" and "T-Shaped" structures, Electric field intensity inside bP in the "Ribbon" structure, Light absorption density in bP in the "Cross" structure, Details of geometrical parameters optimization

References

(1) Giannini, V.; Fernandez-Dominguez, A. I.; Heck, S. C.; Maier, S. A. Plasmonic Nanoantennas: Fundamentals and Their Use in Controlling the Radiative Properties of Nanoemitters. *Chem. Rev.* **2011**, *111*, 3888–3912.

(2) Wang, D.; Zhu, W.; Chu, Y.; Crozier, K. B. High Directivity Optical Antenna Substrates for Surface Enhanced Raman Scattering. *Adv. Mater.* **2012**, *24*, 4376–4380.

(3) Kinkhabwala, A.; Yu, Z.; Fan, S.; Avlasevich, Y.; Mullen, K.; Moerner, W. E. Large Single-Molecule Fluorescence Enhancements Produced by a Bowtie Nanoantenna. *Nat. Photonics* **2009**, *3*, 654–657.

(4) Neubrech, F.; Huck, C.; Weber, K.; Pucci, A.; Giessen, H. Surface-Enhanced Infrared Spectroscopy Using Resonant Nanoantennas. *Chem. Rev.* **2017**, *117*, 5110–5145.

(5) Wang, H.; Li, S.; Ai, R.; Huang, H.; Shao, L.; Wang, J. Plasmonically Enabled Two-Dimensional Material-Based Optoelectronic Devices. *Nanoscale* **2020**, *12*, 8095–8108.

(6) Li, X.; Zhu, J.; Wei, B. Hybrid Nanostructures of Metal/Two-Dimensional Nanomaterials for Plasmon-Enhanced Applications. *Chem. Soc. Rev.* **2016**, *45*, 3145–3187.

(7) Azar, N. S.; Shrestha, V. R.; Crozier, K. B. Bull's Eye Grating Integrated with Optical Nanoantennas for Plasmonic Enhancement of Graphene Long-Wave Infrared Photodetectors. *Appl. Phys. Lett.* **2019**, *114*, 091108.

(8) Yao, Y.; Shankar, R.; Rauter, P.; Song, Y.; Kong, J.; Loncar, M.; Capasso, F. High-Responsivity Mid-Infrared Graphene Detectors with Antenna-Enhanced Photocarrier Generation and Collection. *Nano Lett.* **2014**, *14*, 3749–3754.

(9) Xia, F.; Wang, H.; Xiao, D.; Dubey, M.; Ramasubramaniam, A. Two-Dimensional Material Nanophotonics. *Nat. Photonics* **2014**, *8*, 899–907.

(10) Koppens, F. H. L.; Mueller, T.; Avouris, P.; Ferrari, A. C.; Vitiello, M. S.; Polini, M. Photodetectors Based on Graphene, Other Two-Dimensional Materials and Hybrid Systems. *Nat. Nanotechnol.* **2014**, *9*, 780–793.

(11) Xie, C.; Mak, C.; Tao, X.; Yan, F. Photodetectors Based on Two-Dimensional Layered Materials Beyond Graphene. *Adv. Funct. Mater.* **2017**, *27*, 1603886.

(12) Mak, K. F.; Shan, J. Photonics and Optoelectronics of 2D Semiconductor Transition Metal Dichalcogenides. *Nat. Photonics* **2016**, *10*, 216–226.

(13) Sun, Z.; Chang, H. Graphene and Graphene-Like Two-Dimensional Materials in Photodetection: Mechanisms and Methodology. *ACS Nano* **2014**, *8*, 4133–4156.

(14) Chen, H.; Liu, H.; Zhang, Z.; Hu, K.; Fang, X. Nanostructured Photodetectors: From Ultraviolet to Terahertz. *Adv. Mater.* **2016**, *28*, 403–433.

(15) Chen, X.; Lu, X.; Deng, B.; Sinai, O.; Shao, Y.; Li, C.; Yuan, S.; Tran, V.; Watanabe, K.; Taniguchi, T.; Naveh, D.; Yang, L.; Xia, F. Widely Tunable Black Phosphorus Mid-Infrared Photodetector. *Nat. Commun.* **2017**, *8*, 1–7.

(16) Guo, Q.; Pospischil, A.; Bhuiyan, M.; Jiang, H.; Tian, H.; Farmer, D.; Deng, B.; Li, C.; Han, S.-J.; Wang, H.; Xia, Q.; Ma, T.-P.; Mueller, T.; Xia, F. Black Phosphorus Mid-Infrared Photodetectors with High Gain. *Nano Lett.* **2016**, *16*, 4648–4655.

(17) Ross, J. S.; Klement, P.; Jones, A. M.; Ghimire, N. J.; Yan, J.; Mandrus, D. G.; Taniguchi, T.; Watanabe, K.; Kitamura, K.; Yao, W.; Cobden, D. H.; Xu, X. Electrically Tunable Excitonic Light-Emitting Diodes Based on Monolayer WSe_2 p-n Junctions. *Nat. Nanotechnol.* **2014**, *9*, 268–272.

(18) Zhang, Y. J.; Oka, T.; Suzuki, R.; Ye, J. T.; Iwasa, Y. Electrically Switchable Chiral Light-Emitting Transistor. *Science* **2014**, *344*, 725–728.

(19) Cheng, R.; Li, D.; Zhou, H.; Wang, C.; Yin, A.; Jiang, S.; Liu, Y.; Chen, Y.; Huang, Y.; Duan, X. Electroluminescence and Photocurrent Generation from Atomically Sharp WSe_2/MoS_2 Heterojunction p-n Diodes. *Nano Lett.* **2014**, *14*, 5590–5597.

(20) Zeng, B.; Huang, Z.; Singh, A.; Yao, Y.; Azad, A. K.; Mohite, A. D.; Taylor, A. J.; Smith, D. R.; Chen, H.-T. Hybrid Graphene Metasurfaces for High-Speed Mid-Infrared Light Modulation and Single-Pixel Imaging. *Light Sci. Appl.* **2018**, *7*, 1–8.

(21) Lin, C.; Grassi, R.; Low, T.; Helmy, A. S. Multilayer Black Phosphorus as a Versatile Mid-Infrared Electro-Optic Material. *Nano Lett.* **2016**, *16*, 1683–1689.

(22) Venuthurumilli, P. K.; Ye, P. D.; Xu, X. Plasmonic Resonance Enhanced Polarization-Sensitive Photodetection by Black Phosphorus in Near Infrared. *ACS Nano* **2018**, *12*, 4861–4867.

(23) Fang, Z.; Liu, Z.; Wang, Y.; Ajayan, P. M.; Nordlander, P.; Halas, N. J. Graphene-Antenna Sandwich Photodetector. *Nano Lett.* **2012**, *12*, 3808–3813.

(24) Chen, Z.; Li, X.; Wang, J.; Tao, L.; Long, M.; Liang, S.-J.; Ang, L. K.; Shu, C.; Tsang, H. K.; Xu, J.-B. Synergistic Effects of Plasmonics and Electron Trapping in Graphene Short-Wave Infrared Photodetectors with Ultrahigh Responsivity. *ACS Nano* **2017**, *11*, 430–437.

(25) Kern, J.; Trugler, A.; Niehues, I.; Ewering, J.; Schmidt, R.; Schneider, R.; Najmaei, S.; George, A.; Zhang, J.; Lou, J.; Hohenester, U.; de Vasconcellos, S. M.; Bratschitsch, R. Nanoantenna-Enhanced Light-Matter Interaction in Atomically Thin WS_2. *ACS Photonics* **2015**, *2*, 1260–1265.

(26) Degl'Innocenti, R.; Xiao, L.; Jessop, D. S.; Kindness, S. J.; Ren, Y.; Lin, H.; Zeitler, J. A.; Alexander-Webber, J. A.; Joyce, H. J.; Braeuninger-Weimer, P.; Hofmann, S.; Beere, H. E.; Ritchie, D. A. Fast Room-Temperature Detection of Terahertz

Quantum Cascade Lasers with Graphene-Loaded Bow-Tie Plasmonic Antenna Arrays. *ACS Photonics* **2016**, *3*, 1747–1753.

(27) Tahersima, M. H. et al. Testbeds for Transition Metal Dichalcogenide Photonics: Efficacy of Light Emission Enhancement in Monomer vs Dimer Nanoscale Antennae. *ACS Photonics* **2017**, *4*, 1713–1721.

(28) Lee, B.; Park, J.; Han, G. H.; Ee, H.-S.; Naylor, C. H.; Liu, W.; Johnson, A. C.; Agarwal, R. Fano Resonance and Spectrally Modified Photoluminescence Enhancement in Monolayer MoS_2 Integrated with Plasmonic Nanoantenna Array. *Nano Lett.* **2015**, *15*, 3646–3653.

(29) Butun, S.; Tongay, S.; Aydin, K. Enhanced Light Emission from Large-Area Monolayer MoS_2 Using Plasmonic Nanodisc Arrays. *Nano Lett.* **2015**, *15*, 2700–2704.

(30) Cheng, F.; Johnson, A. D.; Tsai, Y.; Su, P.-H.; Hu, S.; Ekerdt, J. G.; Shih, C.-K. Enhanced Photoluminescence of Monolayer WS_2 on Ag Films and Nanowire-WS_2-Film Composites. *ACS Photonics* **2017**, *4*, 1421–1430.

(31) Cai, T.; Kim, J.-H.; Yang, Z.; Dutta, S.; Aghaeimeibodi, S.; Waks, E. Radiative Enhancement of Single Quantum Emitters in WSe_2 Monolayers Using Site-Controlled Metallic Nanopillars. *ACS Photonics* **2018**, *5*, 3466–3471.

(32) Wang, Z.; Dong, Z.; Gu, Y.; Chang, Y.-H.; Zhang, L.; Li, L.-J.; Zhao, W.; Eda, G.; Zhang, W.; Grinblat, G.; Maier, S. A.; Yang, J. K.; Qiu, C.-W.; Wee, A. T. Giant Photoluminescence Enhancement in Tungsten-Diselenide-Gold Plasmonic Hybrid Structures. *Nat. Commun.* **2016**, *7*, 1–8.

(33) Najmaei, S.; Mlayah, A.; Arbouet, A.; Girard, C.; Leotin, J.; Lou, J. Plasmonic Pumping of Excitonic Photoluminescence in Hybrid MoS_2-Au Nanostructures. *ACS Nano* **2014**, *8*, 12682–12689.

(34) Sortino, L.; Zotev, P.; Mignuzzi, S.; Cambiasso, J.; Schmidt, D.; Genco, A.; Abmann, M.; Bayer, M.; Maier, S. A.; Sapienza, R.; Tartakovskii, A. Enhanced Light-Matter Interaction in an Atomically Thin Semiconductor Coupled with Dielectric Nano-Antennas. *Nat. Commun.* **2019**, *10*, 1–8.

(35) Amani, M.; Tan, C.; Zhang, G.; Zhao, C.; Bullock, J.; Song, X.; Kim, H.; Shrestha, V. R.; Gao, Y.; Crozier, K. B.; Scott, M.; Javey, A. Solution-Synthesized High-Mobility Tellurium Nanoflakes for Short-Wave Infrared Photodetectors. *ACS Nano* **2018**, *12*, 7253–7263.

(36) Engel, M.; Steiner, M.; Lombardo, A.; Ferrari, A. C.; Lohneysen, H. V.; Avouris, P.; Krupke, R. Light-Matter Interaction in a Microcavity-Controlled Graphene Transistor. *Nat. Commun.* **2012**, *3*, 1–6.

(37) Thareja, V.; Kang, J.-H.; Yuan, H.; Milaninia, K. M.; Hwang, H. Y.; Cui, Y.; Kik, P. G.; Brongersma, M. L. Electrically Tunable Coherent Optical Absorption in Graphene with Ion Gel. *Nano Lett.* **2015**, *15*, 1570–1576.

(38) Luo, Y.; Shepard, G. D.; Ardelean, J. V.; Rhodes, D. A.; Kim, B.; Barmak, K.; Hone, J. C.; Strauf, S. Deterministic Coupling of Site-Controlled Quantum Emitters in Monolayer WSe_2 to Plasmonic Nanocavities. *Nat. Nanotechnol.* **2018**, *13*, 1137–1142.

(39) Kleemann, M.-E.; Chikkaraddy, R.; Alexeev, E. M.; Kos, D.; Carnegie, C.; Deacon, W.; de Pury, A. C.; GroBe, C.; de Nijs, B.; Mertens, J.; Tartakovskii, A. I.; Baumberg, J. J. Strong-Coupling of WSe_2 in Ultra-Compact Plasmonic Nanocavities at Room Temperature. *Nat. Commun.* **2017**, *8*, 1–7.

(40) Liu, H.; Du, Y.; Deng, Y.; Peide, D. Y. Semiconducting Black Phosphorus: Synthesis, Transport Properties and Electronic Applications. *Chem. Soc. Rev.* **2015**, *44*, 2732–2743.

(41) Xia, F.; Wang, H.; Jia, Y. Rediscovering Black Phosphorus as an Anisotropic Layered Material for Optoelectronics and Electronics. *Nat. Commun.* **2014**, *5*, 1–6.

(42) Bullock, J.; Amani, M.; Cho, J.; Chen, Y.-Z.; Ahn, G. H.; Adinolfi, V.; Shrestha, V. R.; Gao, Y.; Crozier, K. B.; Chueh, Y.-L.; Javey, A. Polarization-Resolved Black Phosphorus/Molybdenum Disulfide Mid-Wave Infrared Photodiodes with High Detectivity at Room Temperature. *Nat. Photonics* **2018**, *12*, 601–607.

(43) Ye, L.; Li, H.; Chen, Z.; Xu, J.-B. Near-Infrared Photodetector Based on MoS_2/Black Phosphorus Heterojunction. *ACS Photonics* **2016**, *3*, 692–699.

(44) Deng, Y.; Luo, Z.; Conrad, N. J.; Han Liu, Y. G.; Najmaei, S.; Ajayan, P. M.; Lou, J.; Xu, X.; Ye, P. D. Black Phosphorus-Monolayer MoS_2 van der Waals Heterojunction p-n Diode. *ACS Nano* **2014**, *8*, 8292–8299.

(45) Yan, W.; Shrestha, V. R.; Jeangros, Q.; Azar, N. S.; Balendhran, S.; Ballif, C.; Crozier, K. B.; Bullock, J. Spectrally Selective Mid-Wave Infrared Detection Using Fabry-Perot Cavity Enhanced Black Phosphorus 2D Photodiodes. *ACS Nano* **2020**, *14*, 13645–13651.

(46) Wang, J.; Rousseau, A.; Yang, M.; Low, T.; Francoeur, S.; Kéna-Cohen, S. Mid-Infrared Polarized Emission from Black Phosphorus Light-Emitting Diodes. *Nano Lett.* **2020**, *20*, 3651–3655.

(47) Zhou, Z.; Cui, Y.; Tan, P.-H.; Liu, X.; Wei, Z. Optical and Electrical Properties of Two-Dimensional Anisotropic Materials. *J. Semicond.* **2019**, *40*, 061001.

(48) Wang, J.; Rousseau, A.; Eizner, E.; Phaneuf-L'Heureux, A.-L.; Schue, L.; Francoeur, S.; Kéna-Cohen, S. Spectral Responsivity and Photoconductive Gain in Thin Film Black Phosphorus Photodetectors. *ACS Photonics* **2019**, *6*, 3092–3099.

(49) Tong, L. et al. Stable Mid-Infrared Polarization Imaging Based on Quasi-2D Tellurium at Room Temperature. *Nat. Commun.* **2020**, *11*, 1–10.

(50) Dopf, K.; Moosmann, C.; Kettlitz, S. W.; M, P.; Schwab,; Ilin, K.; Siegel, M.; Lemmer, U.; Eisler, H.-J. Coupled T-Shaped Optical Antennas with Two Resonances Localized in a Common Nanogap. *ACS Photonics* **2015**, *2*, 1644–1651.

(51) Liu, J.-M. *Principles of Photonics*; Cambridge University Press, 2016.

(52) Morita, A. Semiconducting Black Phosphorus. *Appl. Phys. A* **1986**, *39*, 227–242.

(53) Ling, X.; Wang, H.; Huang, S.; Xia, F.; Dresselhaus, M. S. The Renaissance of Black Phosphorus. *Proc. Natl. Acad. Sci. U.S.A.* **2015**, *112*, 4523–4530.

(54) Purcell, E. M. Spontaneous Emission Probabilities at Radio Frequencies. *Phys. Rev.* **1946**, *69*, 681.

(55) Pelton, M. Modified Spontaneous Emission in Nanophotonic Structures. *Nat. Photonics* **2015**, *9*, 427–435.

(56) Long, L.; Niu, X.; Yan, K.; Zhou, G.; Wang, J.; Wu, X.; Chu, P. K. Highly Fluorescent and Stable Black Phosphorus Quantum Dots in Water. *Small* **2018**, *14*, 1803132.

(57) Taflove, A.; Hagness, S. C. *Computational Electrodynamics: The Finite-Difference Time-Domain Method*; Artech house, 2005.

(58) Kischkat, J.; Peters, S.; Gruska, B.; Semtsiv, M.; Chashnikova, M.; Klinkmuller, M.; Fedosenko, O.; Machulik, S.; Aleksandrova, A.; Monastyrskyi, G.; Flores, Y.; Masselink, W. T. Mid-Infrared Optical Properties of Thin Films of Aluminum Oxide, Titanium Dioxide, Silicon Dioxide, Aluminum Nitride, and Silicon Nitride. *Appl. Opt.* **2012**, *51*, 6789–6798.

(59) Palik, E. D. *Handbook of Optical Constants of Solids*; Academic press, 1998; Vol. 3.

Graphical TOC Entry

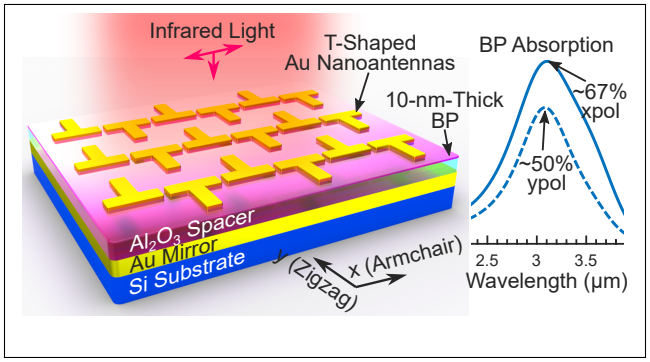

Light-Matter Interaction Enhancement in Anisotropic 2D Black Phosphorous via Polarization-Tailoring Nano-Optics

Nima Sefidmooye Azar, James Bullock, Sivacarendran Balendhran, Hyungjin Kim, Ali Javey, and Kenneth B. Crozier

This graphic illustrates the proposed "T-Shaped" structure together with the obtained result. The graphic shows that, using this structure, the infrared light absorption in a 10-nm-thick bP can reach as high as ∼67% and ∼50% for x- and y-polarized illumination, respectively.